Oxid Met (2014) 81:373–382
DOI 10.1007/s11085-013-9445-4

ORIGINAL PAPER

Effects of Microstructure and Rare-Earth Constituent on the Oxidation Behavior of Ti–5.6Al–4.8Sn–2Zr–1Mo–0.35Si–0.7Nd Titanium Alloy

S. Z. Zhang · B. Zhou · N. Liu · L. Q. Chen

Received: 7 March 2013 / Revised: 30 May 2013 / Published online: 12 September 2013
© Springer Science+Business Media New York 2013

Abstract The isothermal oxidation behavior in air of high-temperature titanium alloy Ti–5.6Al–4.8Sn–2Zr–1Mo–0.35Si–0.7Nd with bimodal and lamellar microstructures was investigated at 600–800 °C. The results revealed that the alloy with lamellar microstructure has better oxidation resistance than that with bimodal microstructure. The porous oxide scales that form mainly contain TiO_2. A noticeable observation concerns the preferential attack around rare-earth particles, associated rapid oxygen diffusion along the incoherent rare-earth precipitate/matrix interface and cracks formed during oxidation. The resulting internal attack caused fragmentation of rare-earth particles and further oxidation of substrate to form TiO_2 scale with some fine dispersoids of Al_2O_3. Tensile tests showed that the ultimate strength and ductility of the specimens with removed surface were higher than that with a surface scale.

Keywords Near-α titanium alloy · Oxidation · Rare-earth constituent · Microstructure

Introduction

Near-α titanium alloys are the most important class of structural materials for use as compressor component in advanced gas turbine engines [1]. The advantage of these alloys is their low density combined with good high-temperature mechanical

S. Z. Zhang (✉) · B. Zhou · N. Liu
School of Environmental and Materials Engineering, Yantai University, Yantai 264005
People's Republic of China
e-mail: szzhangyt@163.com

L. Q. Chen
State Key Laboratory of Rolling and Automation, Northeastern University, Shenyang 110819,
People's Republic of China

properties [2, 3]. Conventional near-α titanium alloys exhibit excellent creep resistance and structural stability at temperatures up to about 500 °C [4, 5]. However, during long-term exposure to air at temperatures above 550 °C, a highly brittle oxygen-contaminated surface α case forms and its formation is a major cause of severe degradation of tensile ductility and fatigue resistance, [6, 7] which substantially limits the high-temperature capability during service and hinders commercial application [8, 9]. The oxidation behavior of titanium alloys is strongly affected by such variables as oxidizing environment, microstructure and alloying additions [10–13].

Near-α titanium alloys of optimized chemistry have made it possible to increase the service temperature up to 600 °C [14–16]. Ti–5.6Al–4.8Sn–2Zr–1Mo–0.35Si–0.7Nd, belonging to this category of alloys, contains a significant amount of Nd, which is beneficial to the mechanical properties [17]. The solubility of Nd in a titanium alloy is limited and Nd addition leads to formation of a rare-earth constituent consisting of SnO and Nd_3Sn [18]. Interaction of alloys with oxygen is critical to service life and high-temperature oxidation behavior should be taken into consideration. The oxidation behavior of experimental alloys was investigated in this paper with the aim to gain a better understanding of microstructural stability of the surface layer.

Experimental Procedures

Alloys were prepared by triple vacuum arc remelting. The chemical compositions of these alloys and their α+β/β-transus (β_t) are presented in Table 1. The as-received material was hot rolled at β_t-30 °C to a rod 20 mm in diameter. The samples were then heat-treated at β_t-20 °C or β_t + 15 °C for 2 h and then air cooled to obtain a bimodal or lamellar microstructure, respectively.

Coupons with dimensions of 10 mm × 10 mm × 2 mm were sliced from the slabs. Prior to oxidation testing, all specimens were ground to a 1500-grit finish and degreased in acetone and alcohol. Isothermal air oxidation tests were performed at 600, 700 and 800 °C for 0–100 h followed by air cooling. The oxidation kinetics were determined by discontinuous thermo-gravimetry employing an analytical balance with a resolution of ±10 μg. Constituent phases of the oxide scale were identified by X-ray diffraction (XRD). For metallographic observation, the oxidized samples were cross-sectioned and mounted in an epoxy resin. To prevent scale loss during metallographic preparation, sample surfaces were successively electrolytically deposited with a layer of Ni. Surfaces and cross-sections of the oxidized

Table 1 Chemical compositions and α+β/β-transus temperature (β_t) of the experimental alloys

Alloy	Composition (wt%)							β_t (°C)
	Al	Sn	Zr	Mo	Si	Nd	Ti	
I	5.56	4.74	1.87	1.0	0.38	0.66	Bal.	1,045
II	6.20	4.79	1.95	1.02	0.36	0.67	Bal.	1,050

specimens were studied with a JSM-6301F scanning electron microscope (SEM). A set of tensile samples after 100 h exposure at 600 and 650 °C were machined to remove the oxygen-contaminated surface α case. Specimens having 5 mm gage diameter and 25 mm gage length were tested.

Results and Discussion

The typical microstructures of Alloy I after heat-treatment at 1,025 °C (β_t-20 °C) and 1,060 °C (β_t + 15 °C) followed by air cooling are shown in Fig. 1. Recrystallization treatment in the α+β phase field resulted in bimodal microstructure consisting of about 16 % globular primary α in a transformed β matrix. As shown in Fig. 1a, the dark particles are the rare-earth constituent comprised of Nd_3Sn matrix, with a space group of *Pm*3*m* and a lattice parameter of $a = 0.344$ nm, and some small dark blocks of SnO dispersed within the Nd_3Sn matrix [18]. Annealing above the (α+β)/β-transus temperature led to a fully lamellar microstructure exhibiting large β grains (Fig. 1b).

Figure 2 shows the weight gain per unit surface area for the samples oxidized in air as a function of time at different temperatures. It is evident that the two alloys showed similar parabolic oxidation behavior during isothermal oxidation at 600–800 °C. The oxidation rate was found to increase with temperature; however, the oxidation rate increased remarkably at 800 °C. The weight gain of Alloy I was slightly greater than that of Alloy II under the same oxidation conditions due presumably to the lower Al content in Alloy I. As is well known, aluminum occupies substitutional sites in the lattice and causes a contraction of the α-Ti lattice, resulting in a reduction in the volume of interstitial sites available to accept oxygen [7]. Thus, aluminum promotes a reduction in the amount of oxygen dissolved in the substrate and this reduction is larger when the Al content is increased [7].

The two microstructures, i.e. bimodal and lamellar, share common features of oxidation behavior in the temperature range studied. However, the bimodal

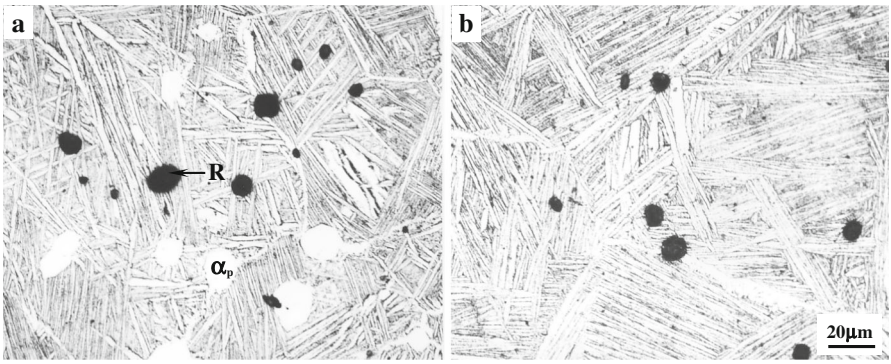

Fig. 1 Optical micrographs showing microstructures of Alloy I, air cooled after heat treatment at 1,025 °C (**a**) and 1,060 °C (**b**) for 2 h. The rare-earth particle is marked by *R*

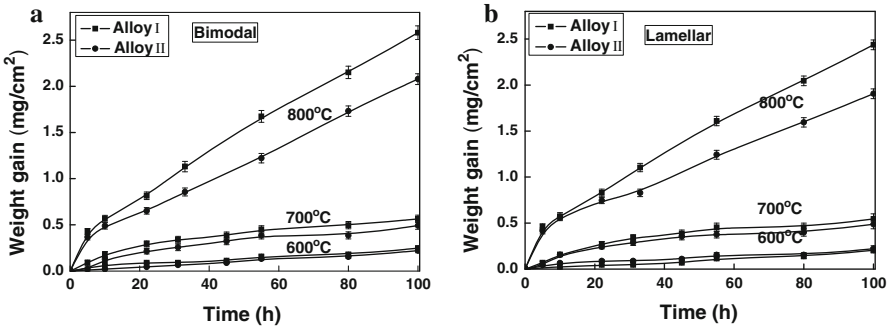

Fig. 2 Weight gain vs time for alloys I and II with bimodal (**a**) and lamellar (**b**) microstructures oxidized in air at different temperature

microstructure exhibited inferior oxidation resistance than the lamellar microstructure at the same oxidation conditions for both alloys. This was probably due to about 16 % primary α phase in the bimodal microstructure. The difference in oxidation behavior is caused by the large difference of oxygen content between the primary α and the β phases. Oxygen is an alpha-stabilizer and very strongly localized in the primary α phase. As a consequence, the primary α rapidly forms a TiO_2 scale when exposed at high temperatures. The oxide layer mainly contains rutile which forms porous scales and the inward diffusion of oxygen through the oxide scales could result in a discontinuous layer re-formation with stronger oxidation. Therefore, about 16 % primary α phase in the bimodal microstructural alloy was mainly responsible for its poor oxidation resistance due to the fast growth of TiO_2.

It is known that grain boundary diffusion becomes dominant below 0.75 to $0.8T_m$ [19]. At the relatively low oxidation temperature tested, mass transport is mainly controlled by diffusion processes along the grain boundaries. The main microstructural characteristic of bimodal to fully lamellar microstructure is the small β grain size (about 40 μm), for which grain boundary is considerably higher. On the other hand, the primary α phases has a higher concentration of oxygen. As a result, a larger number of rapid diffusion paths for oxygen lead to stronger weight gain of bimodal microstructure, but make a smaller contribution to total weight gain.

The oxidation products were identified by XRD and they were similar in the two alloys with two microstructures. The XRD patterns of Alloy I with bimodal microstructure are presented in Fig. 3. The oxide phases are TiO_2 and Al_2O_3, with TiO_2 as the major constituent. Additionally, the patterns contain peaks from the underlying matrix. No ternary phases such as Ti_3AlN were found in the scale at all temperature range in the present study, which differs from the observations of Leyens et al. [11] who also investigated the oxidation behavior of Ti-1100 alloy in the same temperature range. In general, titanium alloys with less than 50 at.% aluminum are not found to form a protective alumina layer during high temperature exposure for thermodynamic reasons, which are well confirmed by many other experimental results [20–22].

Figure 4 shows the SEM micrographs of Alloy I oxidized at 600–800 °C. In all cases, the oxide scales formed on the surface were found to be strongly adherent to

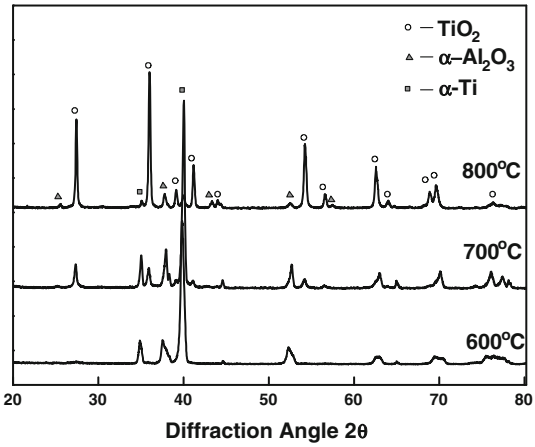

Fig. 3 XRD patterns of oxide scales on Alloy I with bimodal microstructure after oxidation at 600–800 °C for 100 h

the base alloy and appeared multicolored under visual inspection. All the surfaces were covered with porous and heterogeneous oxide scale because the rutile and alumina are mutually insoluble below 1,150 °C [6]. For alloys oxidized at 600 °C, small isolated oxide particles were formed on the surface of the alloys, indicating a slow oxide growth rate. At 700 and 800 °C, the size of oxide crystals increased and the surface was mainly covered with TiO_2 grains. This indicated that besides the inward diffusion of oxygen, the outward diffusion of Ti and Al ions also plays an important role in the formation of the oxide crystals [23].

It is worth noting that the morphologies of rare-earth constituent during oxidation, as is shown in Fig. 5. The rare-earth particles were initially round in shape. At 600 °C, cracks appeared preferentially near edges and corners around the rare-earth constituent (Fig. 5a). As the oxidation temperature was increased to 700 °C, cracks are formed across the whole rare-earth particle (Fig. 5b). A distinct gap was observed between the rare-earth constituent and small particles of oxidation products. At 800 °C, the rutile crystals at the interface of the rare-earth particle and the matrix grew much larger in size (Fig. 5c). The oxidation of rare-earth particles and the formation of internal cracks contributed to their fragmentation. High magnification of rare-earth particle in Fig. 5d shows that there are many small blocks which may be SnO particles dispersed in the Nd_3Sn matrix according to the Ref. [18].

High growth stress arising from local volume changes accompanying oxidation and thermal mismatch stress due to the difference in linear coefficients of thermal expansion between the matrix and rare-earth particle can build up [24]. Initially, the elastic deformation and a small amount of plastic deformation may be sufficient for relieving the stress field. However, continuous oxidation leads to the increase of stress level, so that the plastic deformation is insufficient to relieve the stress field, resulting in the formation of cracks. The formed cracks and incoherent rare-earth precipitate/matrix interface provided rapid diffusion paths for oxygen. As oxygen continues to enter the substrate at a sufficient rate, it provides necessary oxygen supersaturation at the interface of matrix and rare-earth particle, causing further

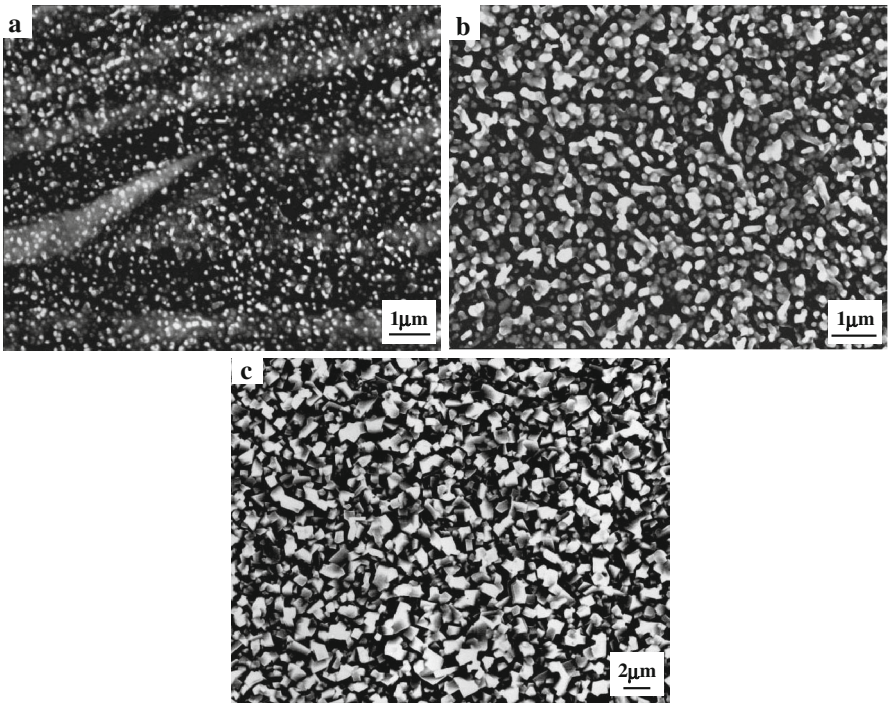

Fig. 4 SEM micrographs of the oxide scale on Alloy I with bimodal microstructure after 100 h of exposure at 600 °C (**a**), 700 °C (**b**) and 800 °C (**c**)

oxidation of substrate to form the TiO_2 and Al_2O_3 scales. As a result, the degradation rate of the material around rare-earth particle was significantly higher.

According to Zhang et al. [25], addition of rare-earth element did not have a significant effect on the oxide scale growth rate, but it can improve the adherence of oxide scale. It has been found[11] that during oxidation of Ti-1100 at 750 °C the oxide scale have poor adherence to the base metal,resulting in strong spallation. However, no clear indication of spallation was observed on the oxide scale near the rare-earth constituent. This can be attributed to the addition of Nd, which can increase the adherence of oxide scales. Detailed characterization of the oxide product for rare-earth constituent is undertaken and will be reported in future communication.

By using SEM with EDS, elemental linear distributions on the oxide surface of Alloy I, including O, are shown in Fig. 6. As is expected, rare-earth particle contained Nd, Sn, and O in substantial amounts, which is in accordance with the reference [18]. However, the O and Al concentration increased suddenly at the interface of rare-earth particle and matrix. The Ti is relatively homogeneous in the matrix excluding rare-earth particle. The elements analysis is consistent with microstructural observations.

Oxide scales in cross section of Alloy I are depicted in Fig. 7. Oxidation produced a porous scale and an oxygen-affected zone. According to Fig. 7a, it was

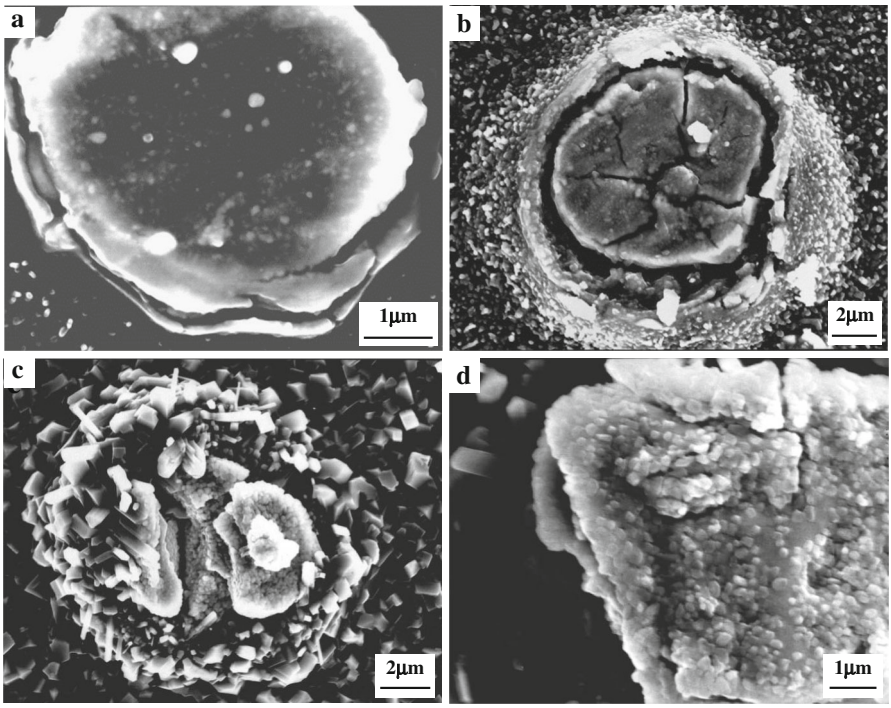

Fig. 5 Morphologies of rare-earth particles in Alloy I with bimodal microstructure after 100 h of exposure at 600 °C (**a**), 700 °C (**b**) and 800 °C (**c**, **d**)

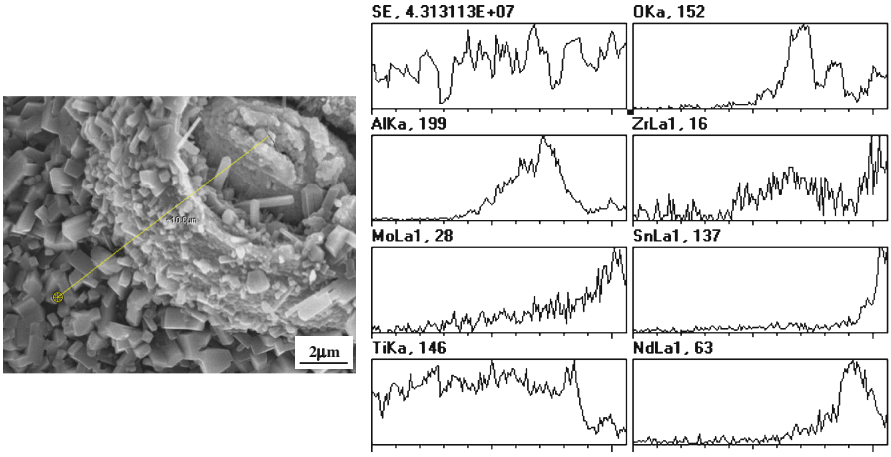

Fig. 6 Elemental distributions on oxide surface of Nd, Sn, O, Ti, Al, Zr, Mo, and Si on Alloy I containing rare-earth particles after 100 h of exposure at 800 °C

clear that the alloy exposed to air at 600 °C for 100 h only presented some small oxide particles with thin oxide scale. After 100 h of exposure at 800 °C (Fig. 7b), the oxide scales showed a significant growth. It is also interesting to note that the

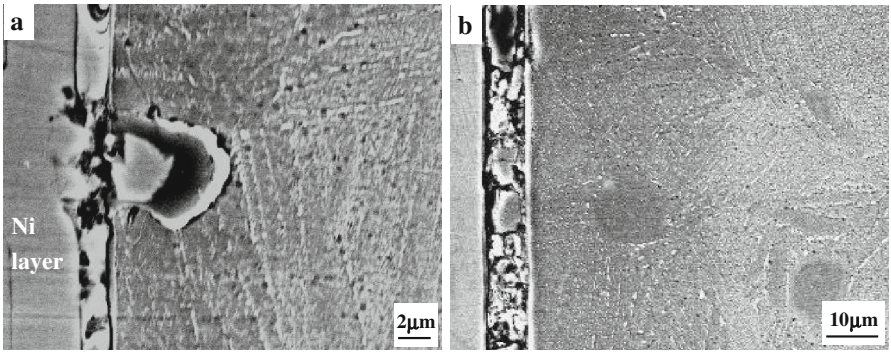

Fig. 7 Cross-sectional SEM micrographs of Alloy I with bimodal microstructure after oxidation at 600 °C (**a**) and 800 °C (**b**) for 100 h

oxidation around rare-earth particle progressively proceeds in depth, as shown in Fig. 7a. Depending on the size of rare-earth particles,the oxide scales could penetrate a depth of several tens of microns below the specimen surface. The average depth of the oxides at these rare-earth particles was about three times that the areas free of rare-earth particles, indicating that the degradation rate at the sites of rare-earth particles can be much higher.

Figure 8 illustrates the effect of surface condition and test temperature on tensile properties of Alloy I after it is exposed at 600 and 650 °C for 100 h. The samples with retained surface have the oxygen-affected surface α case, while the removed surface condition indicates samples with the α case completely removed. It is obvious that the samples with removed surface have higher ultimate tensile strength and ductility than those with retained surface. However, when the test temperature was increased to 240 °C, the α case had almost no effect on ductility. Many tests [26, 27] also confirmed that with the increasing test temperature, the strength decreases whereas the ductility shows the opposite trend.

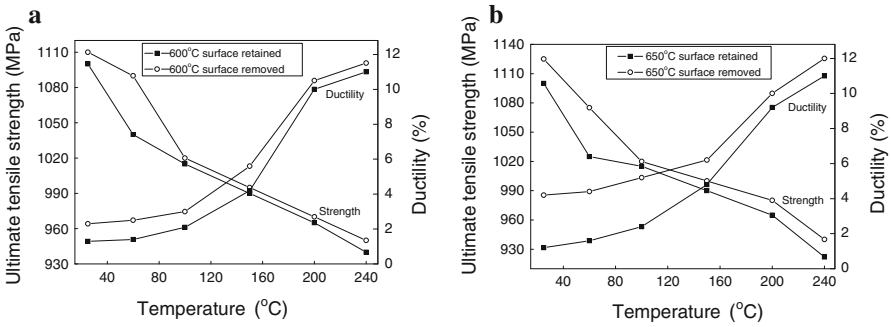

Fig. 8 Variations of room temperature ultimate tensile strength and ductility with exposure temperature for Alloy I with bimodal microstructure after exposure at 600 °C (**a**) and 650 °C (**b**) for 100 h with surface removed and retained

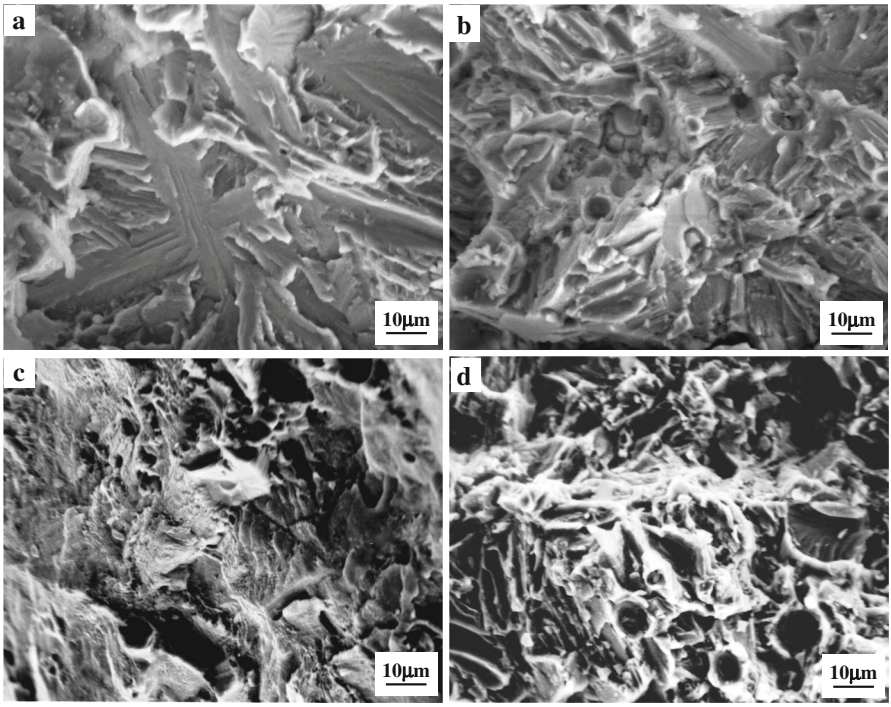

Fig. 9 SEM images of tensile fracture surfaces for Alloy I after exposure at 600 °C for 100 h with surface retained tested at 60 °C and 200 °C. **a** 60 °C, at *edge*, **b** 60 °C, in *middle*, **c** 200 °C, at *edge*, **d** 200 °C, in *middle*

Figure 9 shows the SEM micrographs of tensile fractured surface of Alloy I with retained surface at 60 °C and 200 °C. The fracture topography changed from a transcrystalline fracture, mainly along slip bands at 60 °C, to a transcrystalline, tearing failure with some dimples at 200 °C. At 60 °C, the fracture has a cleavage-like appearance at the edge, and in the middle it mainly shows a brittle manner with little ductile dimple. At 200 °C, the alloy is distinguished by tearing fracture at the edge, and in the middle it shows a mixture of tearing/ductile mode. It is the formation of oxide scale and an oxygen-enriched zone extended into the alloy that lead to a brittle fracture and the samples with retained surface have the lower tensile ductility.

Conclusions

(1) The isothermal oxidation resistance of bimodal microstructure is poorer compared to the fully lamellar microstructure. The oxide scales are porous and mainly contains TiO_2.
(2) The degradation rate of the matrix around rare-earth particle was remarkably higher due to the rapid oxygen diffusion paths along the incoherent rare-earth precipitate/matrix interface and cracks are formed during the oxidation.

(3) The layer around rare-earth particles is TiO_2 scale, with some fine dispersoids of Al_2O_3 and it is strongly adherent to the matrix.
(4) By removing the oxide scales and oxygen-affected zone, better tensile strength and ductility of the alloys can be achieved.

Acknowledgments This work was financially supported by the National Natural Science Foundation of China (Grant No. 50901063), and Science and Technology of Shandong Province, China (Grant No. 2012G0020219).

References

1. J. Williams, *Journal of Materials Processing Technology* **117**, 370–373 (2001).
2. B. Poorganji, M. Yamaguchi, Y. Itsumi, K. Matsumoto, T. Tanaka, Y. Asa, G. Miyamoto and T. Furuhara, *Scripta Materialia* **61**, 419–422 (2009).
3. H. Ghonem, *International Journal of Fatigue* **32**, 1448–1460 (2010).
4. H. Mishra, P. Ghosal, T. K. Nandy and P. K. Saga, *Materials Science and Engineering A* **399**, 222–231 (2005).
5. V. K. Chandravanshi, R. Sarkar, S. V. Kamat and T. K. Nandy, *Journal of Alloys and Compounds* **509**, 5506–5514 (2011).
6. R. G. Reddy, X. Wen and M. Divakar, *Metallurgical and Materials Transactions A: Physical Metallurgy and Materials Science* **32**, 2357–2361 (2001).
7. V. A. C. Haanappel, H. Clemens and M. F. Stroosnijder, *Intermetallics* **10**, 293–305 (2002).
8. M. N. Mungole, N. Singh and G. N. Mathur, *Materials Science and Technology* **18**, 111–114 (2002).
9. I. Gurrapp, *Journal of Alloys and Compounds* **389**, 190–197 (2005).
10. G. Biallas, M. Essert and H. J. Maier, *International Journal of Fatigue* **27**, 1485–1493 (2005).
11. C. Leyens, M. Peters and W. A. Kaysser, *Materials Science and Technology* **12**, 213–218 (1996).
12. H. Garbacz and M. Lewandowska, *Materials Chemistry and Physics* **81**, 542–547 (2003).
13. K. Prasad and V. Kumar, *Materials and Design* **31**, 2716–2724 (2010).
14. P. Wanjara, M. Jahazi, H. Monajati and S. Yue, *Materials Science and Engineering A* **416**, 300–311 (2006).
15. M. Hagiwara and S. Emura, *Materials Science and Engineering A* **352**, 85–92 (2003).
16. Y. F. Han, W. D. Zeng, Y. L. Qi and Y. Q. Zhao, *Materials Science and Engineering A* **529**, 393–400 (2011).
17. G. P. Li, D. Li, Y. Y. Liu, S. X. Guan and Q. J. Wang, *Journal of the Chinese Rare Earth Society* **18**, 341–343 (2000).
18. G. P. Li, D. Li, Y. Y. Liu, Q. J. Wang and Z. Q. Hu, *Metallurgical and Materials Transactions A: Physical Metallurgy and Materials Science* **28**, 1595–1605 (1997).
19. D. Bhattacharyya, G. B. Viswanathan and H. L. Frase, *Acta Materialia* **55**, 6765–6778 (2007).
20. M. Mitoraj, E. Godlewska, O. Heintz, N. Geoffroy, S. Fontana and S. Chevalier, *Intermetallics* **19**, 39–47 (2011).
21. T. Moskalewicz, F. Smeacetto and A. Czyrska-Filemonowicz, *Surface and Coatings Technology* **203**, 2249–2253 (2009).
22. E. H. Copland, B. Gleeson and D. J. Young, *Acta Materialia* **47**, 2937–2949 (1999).
23. M. Mitoraj, E. Godlewska, O. Heintz, N. Geoffroy, S. Fontana and S. Chevalier, *Intermetallics* **19**, 39–47 (2011).
24. S. Z. Zhang, M. M. Li and R. Yang, *Materials Characterization* **62**, 1151–1157 (2011).
25. W. Zhang, G. Chen and Z. Sun, *Scripta Metallurgica et Materialia* **28**, 563–567 (1993).
26. J. Málek, F. Hnilica, J. Veselý, B. Smola, S. Bartáková and J. Vaněk, *Materials Characterization* **66**, 75–82 (2012).
27. S. Malinov, W. Sha and J. J. McKeown, *Computational Materials Science* **21**, 375–394 (2001).